Eruption of prominence initiated by loss of equilibrium: multipoint observations

P. Vemareddy ⬤★ and M. Syed Ibrahim

Indian Institute of Astrophysics, Sarjapur Road, II Block, Koramangala, Bengaluru 560 034, India

ABSTRACT

Using the *SDO*/AIA, *SOHO*/LASCO, *STEREO/SECCHI*, and ground-based H α, radio observations, we studied a prominence eruption (PE) from the western limb that occurred on 2013 December 4. PE is associated with a moderate coronal mass ejection (CME) and GOES class C4.7 flare. Before a couple of days, the prominence pre-existed as an inverse-S shaped filament lying above fragmented opposite polarities between two active regions. Initially, the prominence appears as kinked or writhed as observed from different vantage points. From a careful study of magnetic field observations, we infer that the flux emergence at one leg of the prominence causes the loss of equilibrium which then initiates the slow upward motion of the prominence followed by onset of the eruption at a projected height of 35 Mm. The fast rise motion is also in synchronization with the flare impulsive phase but the average acceleration is quite small ($150\,\mathrm{ms}^{-2}$) compared to strong flare cases. In the LASCO field of view (FOV), the CME continues to accelerate at $3\,\mathrm{ms}^{-2}$ attaining a speed of $450\,\mathrm{km\,s}^{-1}$ at $16\,\mathrm{R}_\odot$. In the extended *STEREO-A* FOV upto $38\,\mathrm{R}_\odot$, the CME decelerates $0.82\,\mathrm{m\,s}^{-2}$. The PE launched type III bursts delayed by 14 min with respect to the flare peak time (04:58 UT). Since the prominence is lying in the fragmented polarities, it is likely that the sheared arcade has little contribution to the poloidal flux of the rising magnetic flux rope and subsequently weak flare is recorded. This study of PE emphasizes the influence of the magnetic reconnection on the CME speed, launch of type II, III burst, and the CME propagation distance farther away from the Sun.

Key words: magnetic fields – solar-terrestrial relations – CMEs – flares – minences – radio bursts.

1 INTRODUCTION

Coronal mass ejections (CMEs) are the most spectacular solar dynamic phenomena that are able to release large amounts of plasma and magnetic field into the heliosphere (Webb & Howard 2012; Zhang et al. 2021). These CMEs in white-light images are observed in association with filament or prominence structures (Webb & Hundhausen 1987; Gopalswamy et al. 2003; Vemareddy, Maurya & Ambastha 2012; Vemareddy, Gopalswamy & Ravindra 2017), X-ray sigmoids (Canfield, Hudson & McKenzie 1999; Moore et al. 2001b; Vasantharaju et al. 2019a), and extreme ultraviolet (EUV) hot channels (Zhang, Cheng & Ding 2012; Cheng et al. 2013; Vemareddy & Zhang 2014; Song et al. 2015; Vemareddy et al. 2022) from the solar dics. In the past two and half decades, although the solar community has made significant progress in understanding the physics of the CMEs, an important aspect of how CMEs are initiated and driven remains elusive (Chen 2011).

The prominence magnetic fields and the initiation mechanisms of the CME eruption are explained by two types of magnetic configuration: one is sheared arcade and the other is flux rope (Forbes & Isenberg 1991; Rust & Kumar 1996; Antiochos, DeVore & Klimchuk 1999; Amari et al. 2003; Mackay et al. 2010). In the flux rope based models the precursor feature such as filament or sigmoid is

regarded as twisted magnetic flux rope (MFR) which is in equilibrium with the overlying arcade field. In this case, the eruption is ensued when the equilibrium is lost by ideal magnetohydrodynamic (MHD) instabilities such as torus instability and/or kink instability (Kliem, Titov & Török 2004; Kliem & Török 2006). In the sheared arcade models, the precursor features are manifested by the sheared and twisted core field and then magnetic reconnection of the shear field lines forms the flux rope which then erupts subsequently (van Ballegooijen & Martens 1989; Moore et al. 2001a).

During the onset of the eruption, the magnetic reconnection induced underneath the uplifting flux rope is seen with the increase of GOES X-ray flux as a flare. The flare impulsive phase is found to be in synchronization with the fast acceleration phase of the flux rope (Zhang et al. 2001; Shanmugaraju et al. 2003; Vršnak et al. 2004). Therefore, the flare magnetic reconnection implies to a feedback mechanism on the CME dynamics (Lin, Soon & Baliunas 2003). It was suggested that the instability plays an important role in triggering and accelerating the MFR, and then the magnetic reconnection accelerates the MFR further and allows the process to develop continuously (Priest & Forbes 2002; Lin, Soon & Baliunas 2003). The analytical study of Vršnak (2016) showed that flare magnetic reconnection reduces the tension of overlying magnetic loops and also adds the poloidal flux to the uplifting flux rope which then increases its hoop force. This aspect was studied in a much closer details with the observations from Atmospheric Imaging Assembly

★ E-mail: vemareddy@iiap.res.in
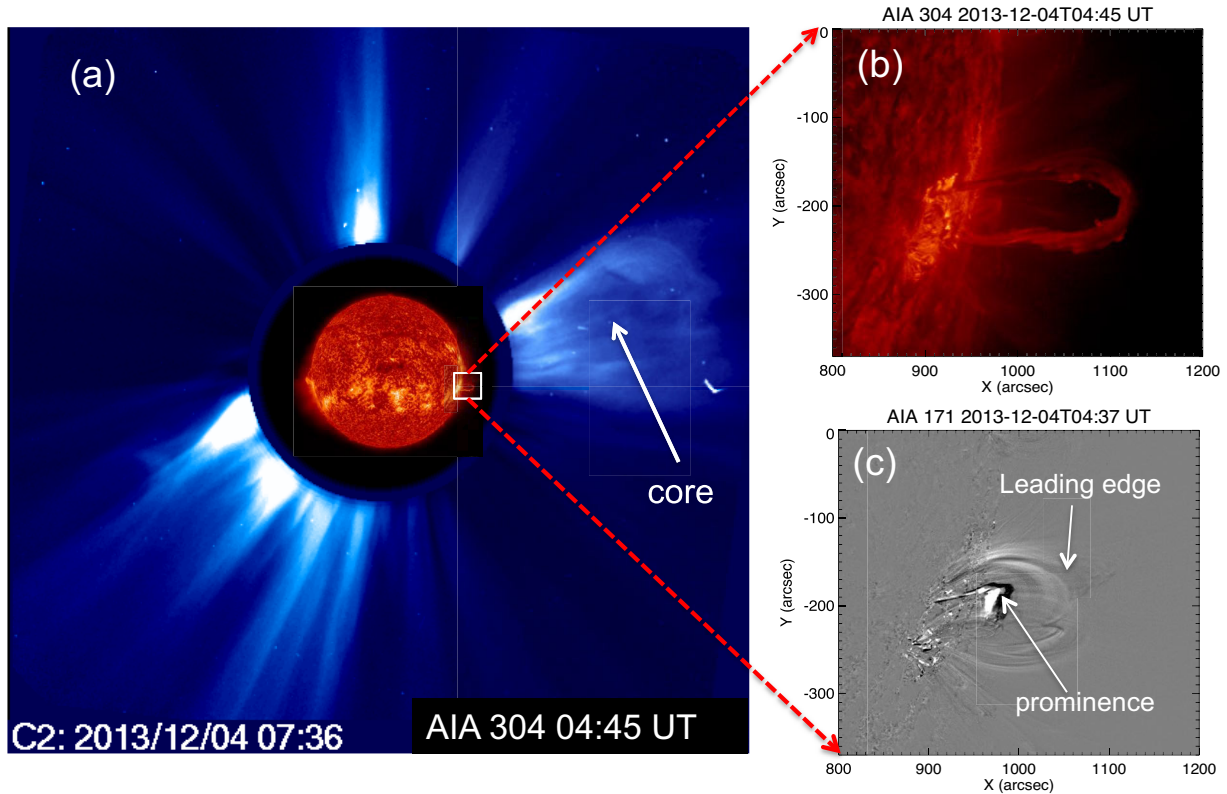
Figure 1. Prominence eruption on 2013 December 4. (a) Combined images of LASCO/C2 and AIA 304Å showing the prominence eruption on west limb has evolved to a white light CME. (b) Magnified image of AIA 304 Å displaying the erupting prominence at 04:45 UT. (c) Magnified running difference image of AIA 193 Å waveband, showing the envelope loop structure as leading edge and core part as prominence.

(AIA; Lemen et al. 2012) onboard *Solar Dynamics Observatory* (*SDO*) in a recent investigation of Vasantharaju et al. (2019b). Their study inferred that flare-associated prominence eruption events have an average acceleration in the range of 400–1550 ms^{-2} and flareless events have an average acceleration well below 200 ms^{-2} during the rapid-acceleration phase. Further such observational studies by (Song et al. 2015, 2018) also suggests that the flare magnetic reconnection contributes equally to the CME acceleration process as ideal MHD instability.

Although there exists several mechanisms of CME initiation in the solar source region, the suitability of a particular mechanism varies from one case to the other, therefore, the CME propagation in the heliosphere is subject to the driver of the CME eruption at the Sun. Also, the radio emissions originating from the erupting source regions differ with the erupting feature, for instance the EUV hot channels are conducive to launch moving type IV radio bursts (Vasanth et al. 2016; Vemareddy et al. 2022). In this study, using the *STEREO* and AIA observations, we present a detailed analysis of the prominence eruption (PE) which occurred on 2013 December 4. The prominence is lying above the fragmented opposite polarities present between two active regions. The mechanism of the eruption process and its influence on the CME propagation was a subject of great interest, which we studied with this event. In Section 2, observations from different instruments are described. The analysis of the eruption process and the CME propagation are presented in Section 3. A summary of the study and discussion is given in Section 4.

2 MULTIPOINT OBSERVATIONS

To study the eruptive prominence on 2013 December 4, we have used the multispacecraft observations from surface of the Sun to inner heliosphere.

The source region observations of the PE are obtained from AIA (Lemen et al. 2012) onboard the *SDO*. AIA provides continuous full-disc observations of the chromosphere and corona in seven EUV channels, spanning a temperature range of around 20 000 K to more than 20 million K. The image stream is 12 s cadence, with $4\,k \times 4\,k$ pixel images at 0.6 arcsec pixel^{-1}, provides unique views of the changing solar outer atmosphere's diverse features. The magnetic field observations of the erupting region are obtained from Helioseismic Magnetic Imager (HMI) onborad the SDO. Fig. 1(b) shows the erupting prominence at the west limb (S09W89) in the AIA 304 Å waveband. Running difference image (Fig. 1c) in AIA 193 Å delineates that the prominence has an envelop of overlying loop system (as leading edge) which is a typical signature of the three-part structure of white-light CME (Illing & Hundhausen 1985).

Fig. 1(a) displays the CME of the erupted prominence observed in the outer corona obtained by Large Angle Spectrometric Coronagraph (LASCO; Brueckner et al. 1995) onboard the *Solar and Heliospheric Observatory* (*SOHO*). LASCO provides white light images in the field of view (FOV) of 2.1–6 (C2), and 3–32 R$_{\odot}$ (C3) to analyse CME dynamics in the near-Sun corona. We have also used the observations from Sun Earth Connection Coronal and Heliospheric Investigation (*SECCHI*; Howard et al. 2008) onboard the *Solar-Terrestrial and Relational Observatory* (*STEREO*; Kaiser
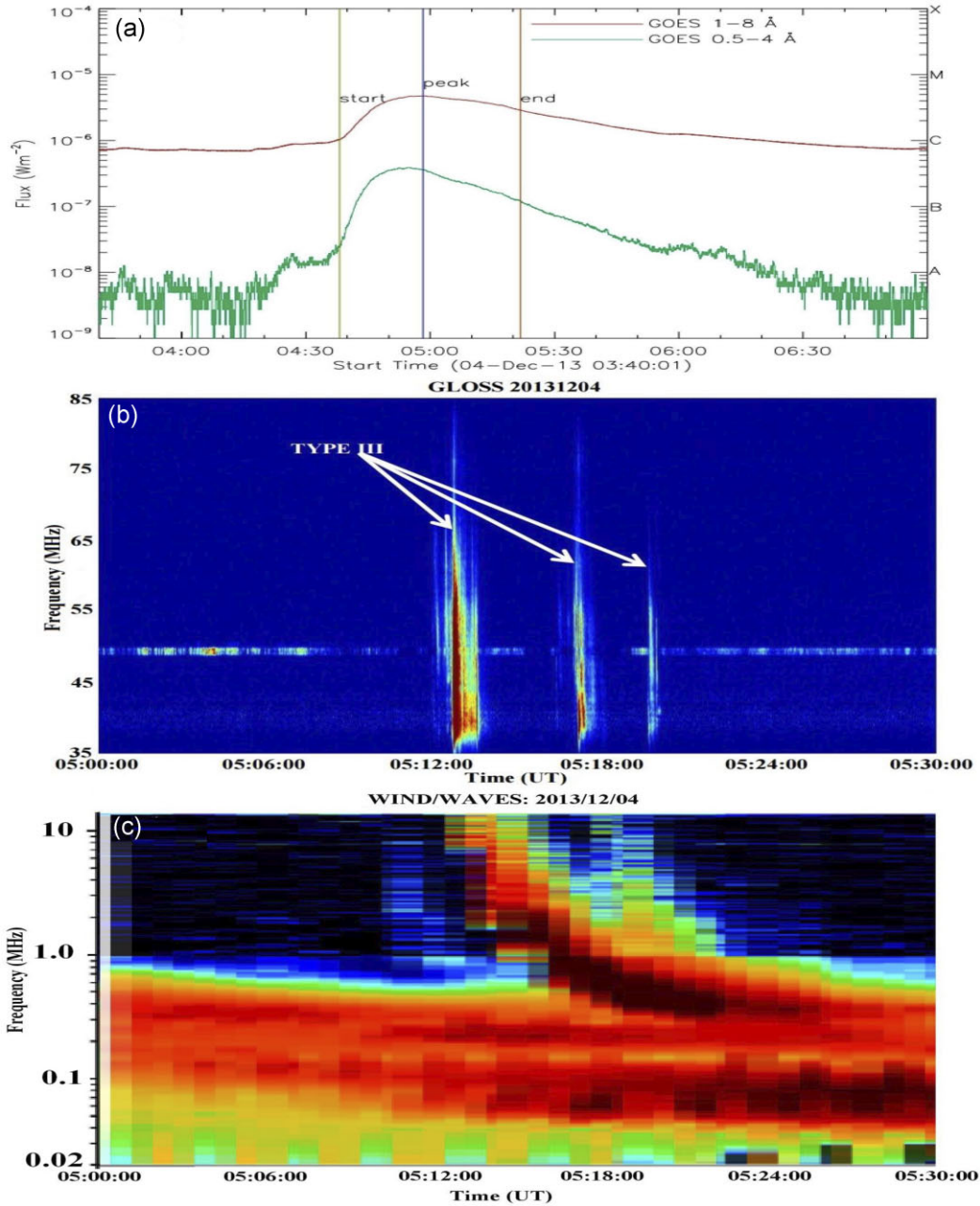
Figure 2. (a) GOES X-ray flux profile showing the associated C4.7 class flare. Flare start, peak, and end times are denoted by green, blue, and red vertical lines, (b) GLOSS dynamic spectrum showing the recurrent radio type III bursts during the flare peak time, and (c) dynamic spectrum obtained by wind/WAVEs delineates the low-frequency type III burst.

et al. 2008) to analyse the CME propagation away from the Sun to inner heliosphere. At the time of this event, the *STEREO-A* (*STA*) has a separation angle of 149.6° with respect to the Earth, therefore the prominence at the west limb from the Earth view will be on the east limb as seen from the *STA*. To study the PE from this *STA* vantage point, we obtained the imaging observations from EUVI, COR1, COR2, and HI1 instruments onboard *STA/SECCHI*.

The PE event is associated to GOES C4.7 class flare as shown in Fig. 2(a), with start time at 04:38 UT and peak time at 04:58 UT. This flare is also accompanied with radio bursts of type III as recorded

by the ground-based radio spectrograph from the Gauribidanur LOw frequency Solar Spectrograph (GLOSS) observations operated by Indian Institute of Astrophysics (IIA) in the *Gauribidanur Observatory* (Kishore et al. 2014) in the metric frequency range of 35–85 MHz (Fig. 2b). In addition, this decametre–hectometric (DH) range observation is also recorded by the space-based radio wind/*WAVES* instrument, which also confirm the type III burst (Bougeret et al. 1995).

We also use H α 6564 Å observations at a pixel size of 1 arcsec and 1 min cadence from the Global Oscillation Network Group (GONG) telescope operating at *Udaipur Solar Observatory*.
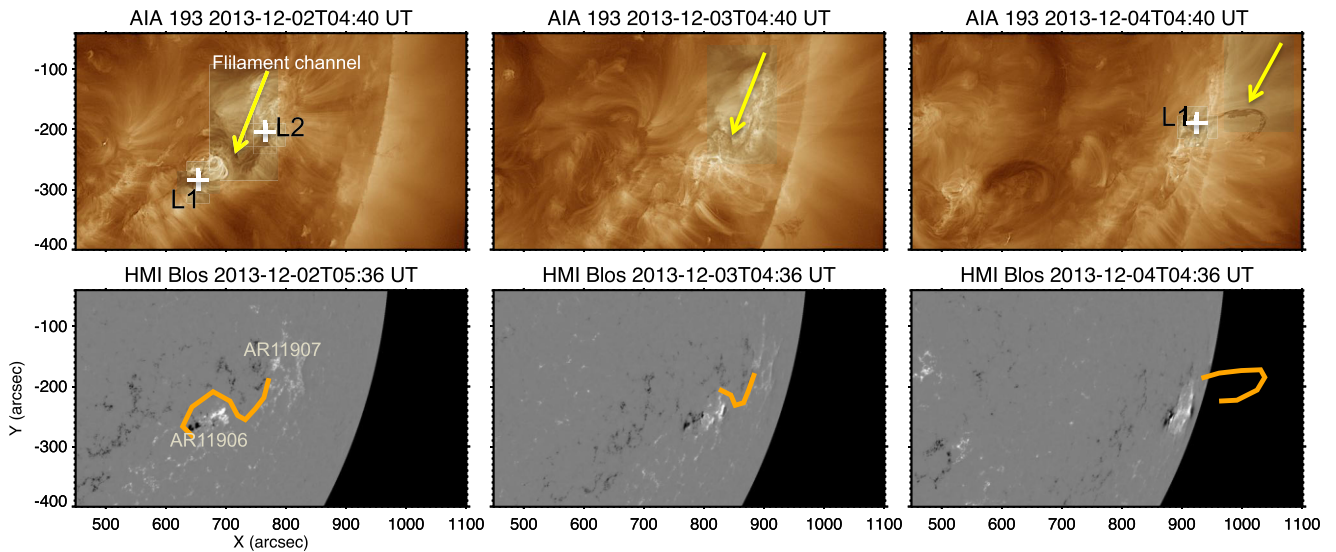
Figure 3. Pre-eruptive observations of the prominence. *Top row panels*: snapshots of the AIA 193 Å showing the filament channel (yellow arrow) before 2 d of the PE. L1 and L2 (plus symbol) marks the legs of the filament. *Bottom row panels*: HMI line-of-sight magnetic field showing the magnetic field distribution on the photospheric surface. The trace of the filament channel (orange curve) is overplotted which is following the interactive region path between AR 11906 and AR 11907. The filament channel apparently resides above the path between opposite polarities.

3 ANALYSIS AND RESULTS

Fig. 3 depicts the co-temporal and co-spatial observations of the HMI magnetic field and AIA snapshots of the corona. A long inverse-S shaped filament channel to the extent of 190 Mm length exists well before 3 d of its eruption between interactive region polarities. On 2013 November 30, the AR 11906 was having fragmented polarities extended upto AR 11907 having much stronger compact polarity regions. The trace of the filament channel (orange curve) observed in AIA 193 Å is overplotted on HMI magnetograms, which implies that the filament channel resides above the polarity inversion line (PIL) between the two ARs. Under the continuous anti-parallel flux motions and the flux cancellations over days, the filament channels have been observed to form along the PIL (e.g. Martin 1998; Gibson 2018) where the chromospheric fibrils are aligned with the polarity boundary.

### 3.1 The eruption process: loss of equilibrium

From the visual inspection of continuous observations in the later evolution till the time of the eruption, it was noticed that the AR 11907 decayed into fragmented polarities whereas the flux emergence occurred in the AR 11906 (bottom panels in Fig. 3). We infer that these conditions of flux imbalance lead to loss of equilibrium of the filament and then its slow rise motion towards the onset of the eruption. While the photosphere continues to evolve with slow flux motions, the filament undergoes numerous stages of adjusting to the surrounding environment. In this process, the prominence begins to activate at 02:00 UT on December 4 and progresses through several stages before reaching the stage of eruption onset at 4:50 UT. During the activation phase, the filament system evolves with quasi-static rise motion such that equilibrium is established with the reorganizing surrounding loops.

In Fig. 4, ground-based GONG H α images and AIA 171 Å images are displayed at different times at the initiation of the eruption. In H α, the prominence appears brighter against the background whereas it is dark in AIA 171 Å images. Especially, the filament segment near leg

L1 is set to rise from 04:20 UT, probably because the magnetic flux emergence at the foot point area. Because of projection effects, we could not produce the flux evolution results to support this inference. From the leg L1, the prominence morphology depicts a helical shape with a dip in the middle section of the corona. This helical shape in the corona implies an inverse-S shape of filament (Rust & Kumar 1994) when seen from top as evidenced on December 2 (Fig. 3). At around 04:38 UT, the kinked prominence stretched and then runs into fast rise motion.

In addition, the prominence rise motion is also captured in the EUV Imager onboard *SECCHI/STA*. Fig. 5 shows the snapshots of the prominence captured in EUVI 304 waveband (left column panels) against the corresponding snapshots acquired from AIA/*SDO*. From the *STA* vantage point, the prominence appears as writhed at 04:36 UT because it is inverse-S shaped from top view. During rise motion, the legs stretch to show the left helical threads in the prominence (white arrow). This implies the left-handed helical nature of magnetic field in the prominence and gives the inverse-S shape morphology as seen from top (Rust & Kumar 1996). Although the prominence appears kinked, the kink-instability as a trigger of this eruption is ruled out. First, the helical threads are not to the extent of critical twist (Török, Kliem & Titov 2004). Second, prominence does not rotate noticeably during its upward rise in the low corona. The apex of rising filaments/prominences with exceeding twist are seen to rotate about the direction of ascent in a clockwise (counterclockwise) direction for positive (negative) or right (left)-handed chirality (Alexander, Liu & Gilbert 2006; Gilbert, Alexander & Liu 2007; Green et al. 2007). Owing to the flux emergence in AR 11906, we suggest that the loss of equilibrium as the cause of eruption in this case.

Along with GOES X-ray flux, the projected height–time measurements of the prominence apex are plotted in Fig. 6. In order to describe the two phase of the eruption, this height–time curve is fitted with a model model containing the linear term to follow the slow rise phase and the exponential term to account for the rapid acceleration phase as described in Cheng et al. (2013) and Vasantharaju et al.
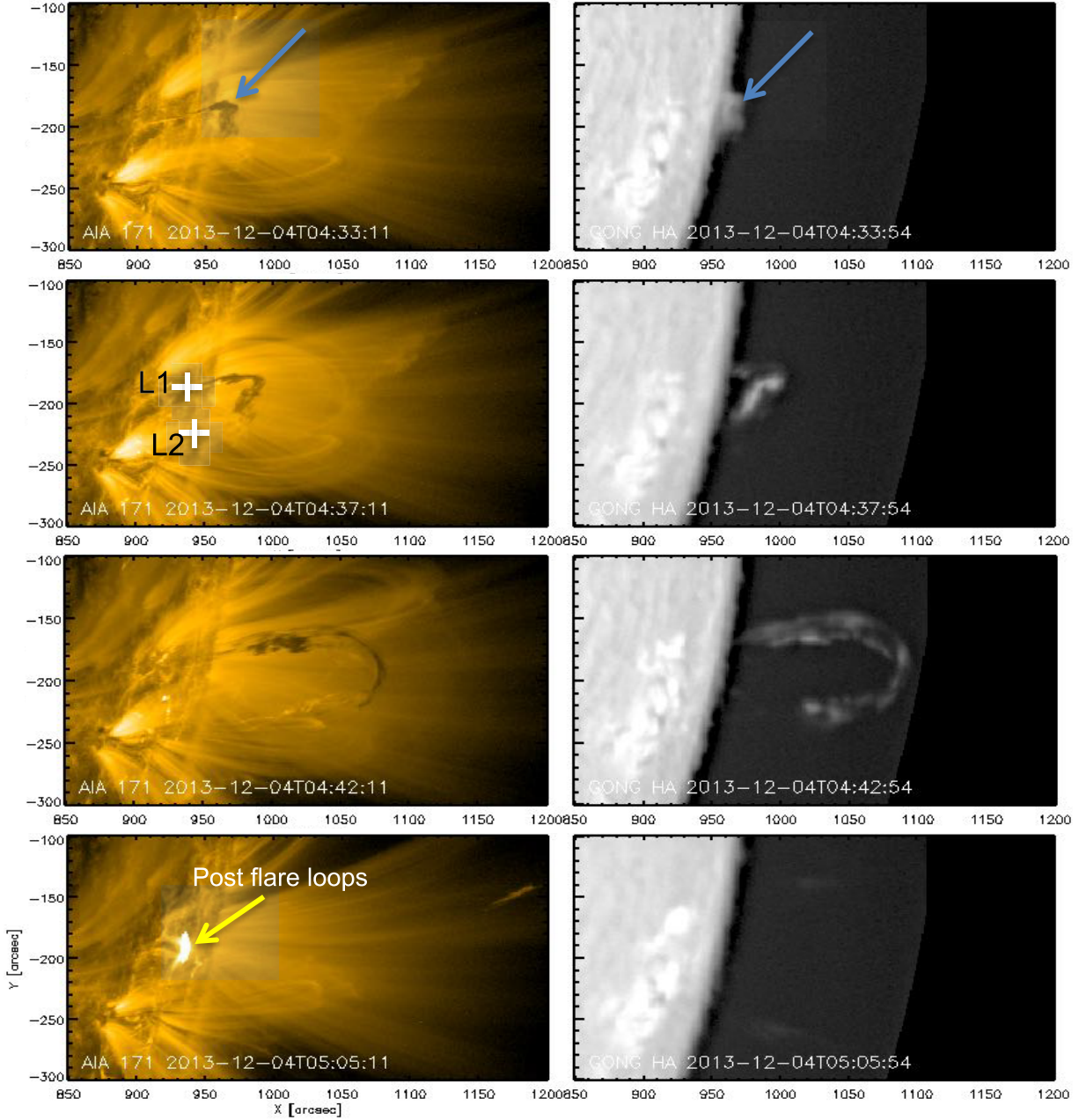
Figure 4. Initiation of the PE on 2013 December 4. *Left column panels*: snapshots of AIA 171 Å show kinked prominence (blue arrow) while it was an inverse-S shaped filament as seen from top three. *Right column panels*: GONG Hα show the kinked prominence as bright feature against the coronal background. At around 04:38 UT, the kinked prominence stretched and then runs into fast rise motion. Post-flare loops form after the eruption. An animation of this figure is available online.

(2019b) and it is given by

$$h(t) = C_0 + C_1 t + C_2 e^{t/\tau}, \tag{1}$$

where C_0, C_1, C_2, and τ are the four free parameters of the fitting. The fitting also gives a straightforward method for determining the commencement of the rapid-acceleration phase as determined by $T_c = \tau ln(C_1\tau/C_0)$. From the fit, we then derived the velocity and acceleration with AIA FOV. Starting at a velocity of 5 km s^{-1}, the slow rise phase continues for 20 min upto 04:38 UT during which the prominence rises from 1.01 to 1.05 Rs. Commencing the main

eruption, in the next 20 min, the prominence rises at a faster phase up to 230 km s^{-1} to a height of 1.28 R$_\odot$. Onset of the main eruption is linked to the strapping effect of overlying flux loops. In the flux rope models of filaments, the strapping effect is weaker at a height defined by critical height roughly 42 Mm in the corona (Filippov & Den 2001; Filippov 2013; Vasantharaju et al. 2018), from where the prominence runs into fast acceleration phase. In this case, the height of fast rise motion (35 Mm) is also in the same height range determined in several prominent cases. Note that the fast rise phase is also in synchronization with the flare impulsive phase, which is a signature of reconnection underneath the ascending prominence and
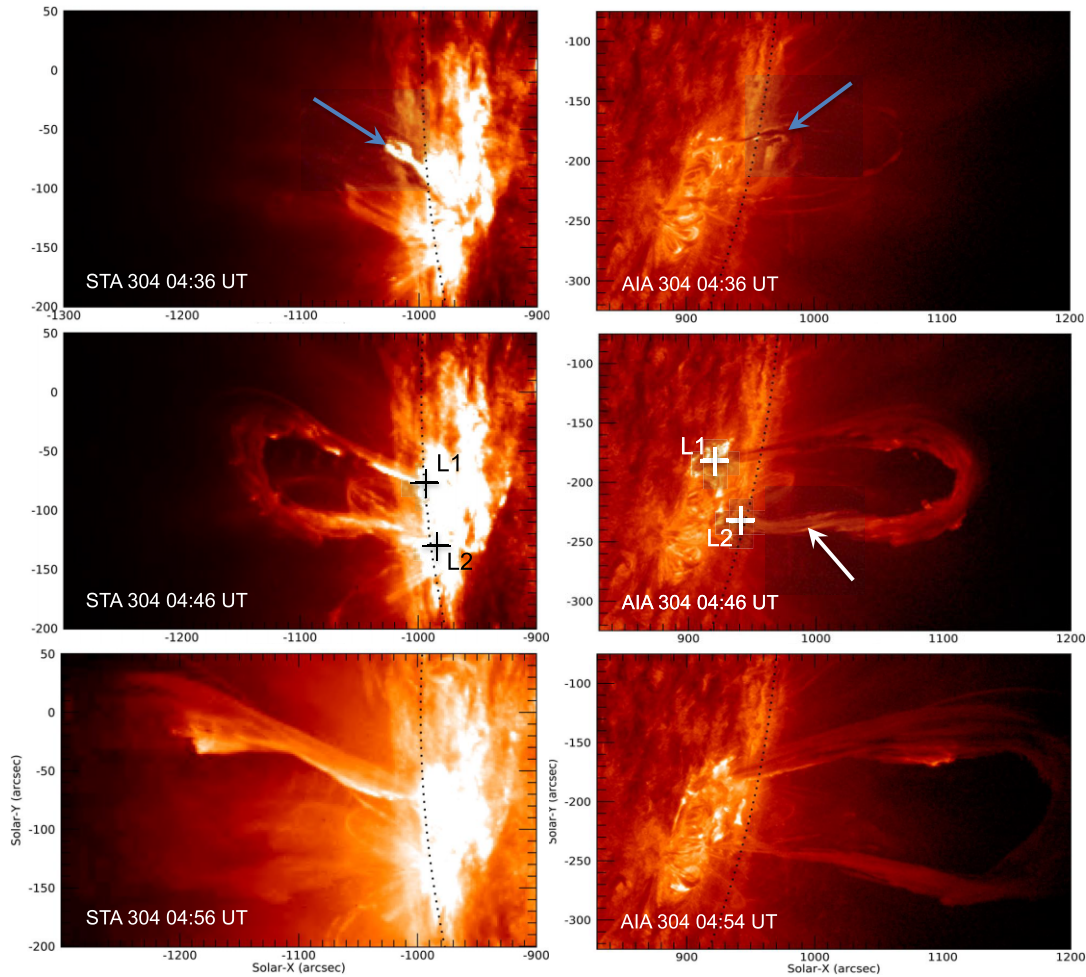
Figure 5. Snapshots of the PE in 304 Å waveband of *SECCHI*/EUVI and *SDO*/AIA. Left column panels show the prominence on east limb whereas right column panels show PE on west limb. Blue arrow points to the same prominence observed as writhed or kinked from different vantage points. Notice the left helical threads (white arrow) along the legs of the prominence. Dotted curve represents the solar limb.
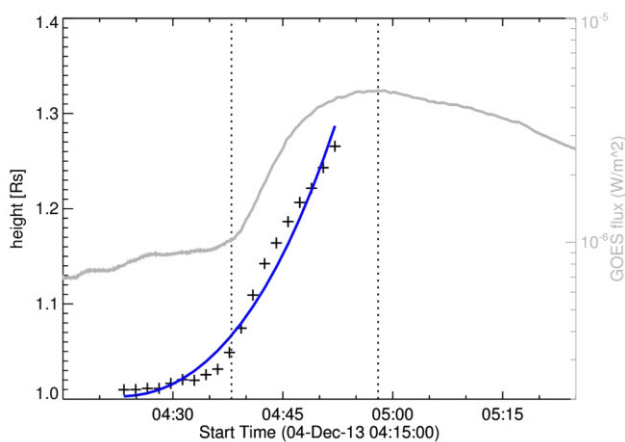

Figure 6. Height of the prominence apex as a function of time. The data points are fitted (blue curve) with a function including linear and exponential terms. GOES X-ray flux (grey) is also plotted with *y*-axis scale on right. Vertical dotted lines denote flare start (04:38 UT) and peak (04:58 UT; C4.7 mag) times. Fast upward rise motion of the prominence synchronizes with the impulsive flare phase.

the resultant post flare loops are observed in AIA hot-channel images (see Fig. 4) located mainly near leg L1.

3.2 Late phase radio emission

Type II bursts are generated from non-thermal electrons produced at the shock front of the CME (Cane, Sheeley & Howard 1987; Gopalswamy, Mäkelä & Yashiro 2019). Since the prominence upward rise speed as well as the CME speed is small (300 km s^{-1}), type II bursts are not observed with this eruptive event.

The flare magnetic reconnection releases huge amounts of magnetic energy some of which turns into kinetic energy which can accelerate electrons to relativistic speeds. These electrons pass through open magnetic field lines from the reconnection point in the corona and then produce type III radio emission (Melrose 1980). As shown in Fig. 2, the radio spectrum present with type III burst starting from 05:12 UT. Three sets of type III emission that GLOSS observed type III a, b, and c are denoted by white arrows. Compared to flare peak time (04:58 UT), the type III burst is delayed by 14 min. We have scrutinized the AIA 171 Å movie carefully and found that the prominence is still in a closed magnetic environment until 04:56 UT. The further upward motion stretches and bends inward
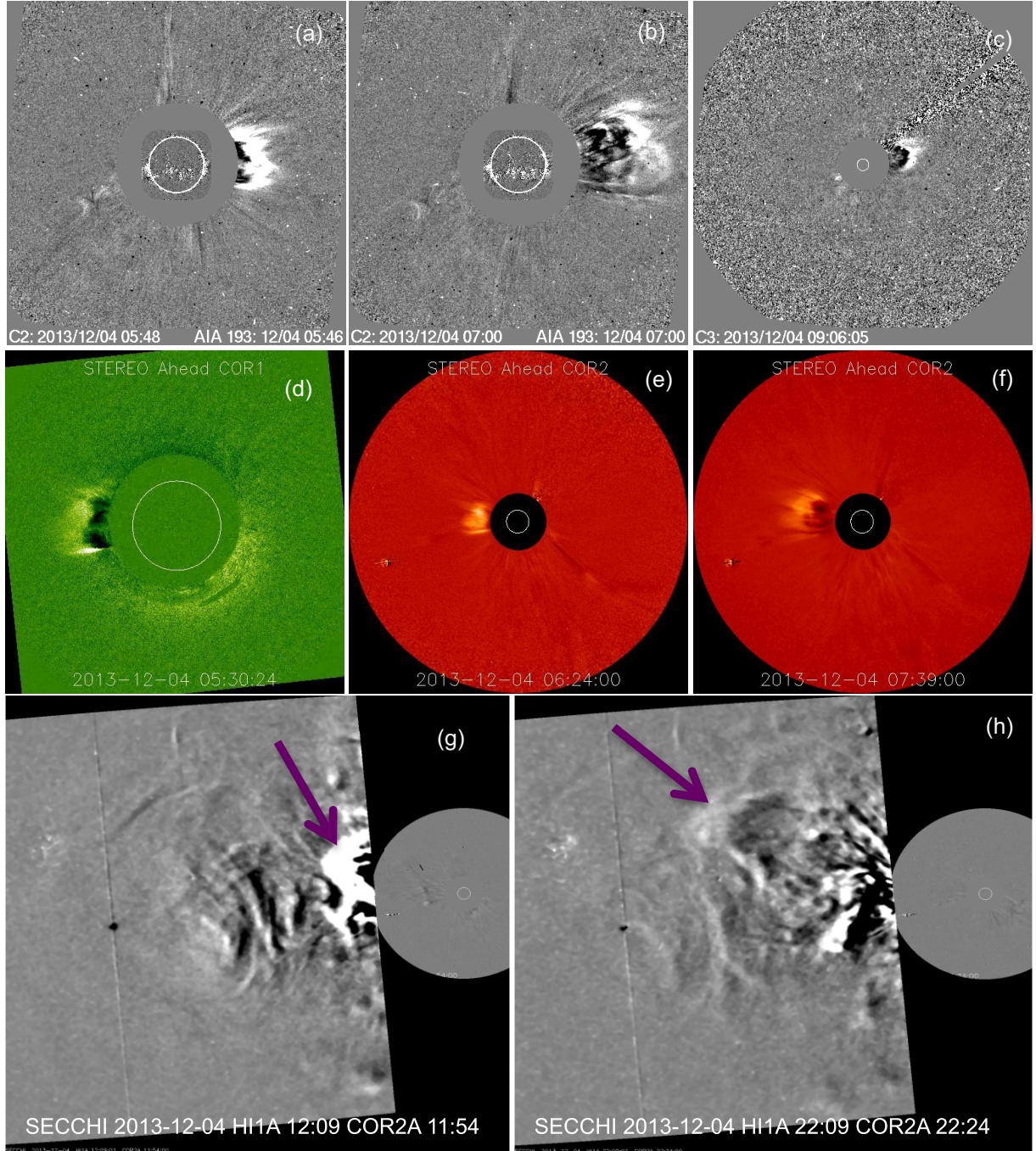
Figure 7. CME propagation from low corona into the heliosphere. (a–c) Running difference coronagraph images of LASCO C2 and C3 showing CME on west side. (d–f) Running difference white-light observations of *STA*/COR1 and *STA*/COR2 showing the same CME on east limb at different epochs. (g–h) Composite running difference images of *STA*/COR2 (2.5–15 $R_\odot$) and *STA*/HI1 (15–90 $R_\odot$) on 2013 December 4. Magenta arrow points to the leading edge of the CME at different epochs of its propagation.

the prominence legs resulting in a late phase post eruption arcade starting from 5:10 UT. In addition to the trapped electrons from the flare impulsive phase, the energetic electrons generated in this late phase likely escaped along open magnetic fields to originate the observed type III bursts. A recent statistical study reports that most of the type III bursts are observed to launch within 20 min of flare peak time (Mahender et al. 2020) and the timing indicate the opening of the magnetic environment confining the erupting feature.

3.3 CME propagation

The erupting prominence seen in AIA becomes large-scale CME and its propagation was recorded by the LASCO and *STA* white-light observations. The top two row panels in Fig. 7 displays the running difference images recorded by the LASCO C2 and C3 from the Earth view and the corresponding images from COR1 and COR2 onboard *STA*. The CME emerged in C2 FOV at 05:12 UT and in COR1 at 04:56 UT where the three part structure is identifiable as

Angle Vs. Time
2013-12-04 00:00, PA 95, D3, STEREO-A
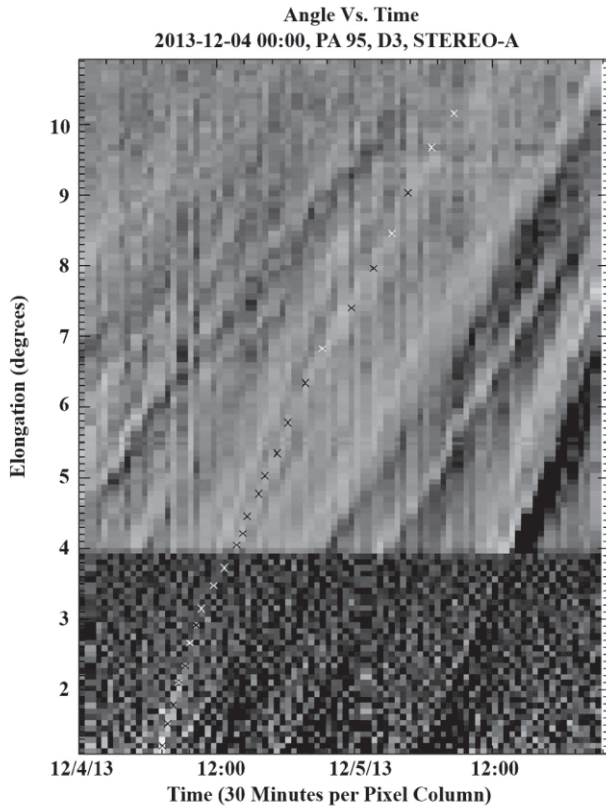
Figure 8. Time-elongation map (J-map) constructed using *STA* white-light observations in COR2 and HI. The CME propagation path is indicated with cross mark symbols up to the distance of ~38.4 $R_\odot$.

noticed in AIA 171 observations (Fig. 1c). The CME is traceable in these middle corona images prominently up to 15 $R_\odot$, and in the later part of evolution, it becomes diffused.

Further evolution of the CME is tracked in the wide angle observations of the Heliospheric Imager-1 (HI1) of *STA*. Fig. 7(g–f) display the composite running images of COR2 and HI1, which show the CME propagation in the outer corona up to 45 $R_\odot$. From these combined images, we constructed time-elongation map (J-map) based on the procedures referred by Sheeley et al. (1999) and Davies et al. (2009). From this J-map, we follow the bright and dark trace of the CME leading edge (' + ' symbols), up to ~11° elongation (equivalent to ~42 $R_\odot$) as shown in Fig. 8.

In the top panel of Fig. 9, we have plotted the projected height–time data of the CME leading edge in the LASCO white-light images as well as the leading edge observed in *STA* coronagraph images. For completeness, the height–time values of the prominence in AIA FOV (Fig. 6) are also included. For the LASCO and *STA* data points, a second order polynomial fit is used. The fitting curves follow the data points with less deviations, so that we can derive quantitative information of CME kinematics more accurately.

In the bottom panel of Fig. 9, we plot the derived velocities from the model fits to the height–time data. GOES X-ray flux is also shown with the *y*-axis scale on the right. In AIA FOV, the prominence rises from 10 to 260 km s^{-1} in a span of 30 min. This fast rise phase corresponds to an average acceleration of 150 ms^{-2}. Note that the velocity curve is also co-temporal with the rise of the GOES X-ray flux, which means the reconnection of overarching loops underneath the rising prominence. In the LASCO FOV, the

velocity of the LE continues to increase from 300 to 453 km s^{-1}, with an acceleration of 3 ms^{-2}. However, in *STA* FOV, the velocity decreases from 327 to 170 km s^{-1} at a deceleration of 0.82 ms^{-2}. Here, it is important to point out the role of the flare reconnection in the rise motion. The prominence is lying above the weak polarities in the periphery of active regions and so the flare reconnection is weak (C4.7) and consequently its feedback on the rising motion of the prominence (Vršnak 2016). For example in a recent study of Vemareddy et al. (2022) the hot-channel eruption leads to M2.4 flare where the hot-channel attained a peak velocity of 400 km s^{-1} at an average acceleration of 600 ms^{-2} within AIA FOV. Combining the LASCO and *STA* fits, it is possible that the CME accelerates up to a certain heliocentric distance and then decelerates further, which is likely due to comparatively lower energy of this CME at its onset.

4 SUMMARY AND DISCUSSION

We studied an interesting PE even from the western limb that occurred on 2013 December 4. It is associated with a weak CME observed in LASCO and *STEREO* white-light images and GOES class C4.7 flare. Before a couple of days, the prominence pre-existed as an inverse-S shaped filament lying above fragmented opposite polarities between two ARs.

At the time of initiation of rise motion, the prominence appears as kinked or writhed as observed from different vantage points. The prominence legs show signatures of magnetic field with left-handed twist but without exceeding critical twist for helical kink instability. From a careful study of magnetic field observations, we infer that the flux emergence at one leg of the prominence causes the loss of equilibrium to initiate the slow rise upward motion.

The initiation of the eruption comprises slow rise motion of the prominence upto 4:38 UT attaining a speed of 90 km s^{-1} at a height of 35 Mm. The fast rise motion attains a speed of 260 km s^{-1} at an average acceleration of 150 ms^{-2} within AIA FOV. Moreover, this fast rise motion is in synchronous with the flare impulsive phase during 04:38-04:58 UT, however owing to the weak magnitude flare, the reconnection underneath appears to have a minor impact on the dynamics of the MFR being ejected. Prominences associated with higher magnitude flares are reported to have higher value of average acceleration during the flare impulsive phase and consequently the CME velocity in LASCO FOV (e.g. Vasantharaju et al. 2019b). Since the prominence is lying in the fragmented polarities, it is likely that the reconnection beneath contributes little to the poloidal flux of the rising MFR (Vršnak 2016).

The CME propagation is tracked in LASCO and HI1/*STA* FOV up to 45 R$_\odot$. In the LASCO FOV, the CME continues to accelerate at 3 ms^{-2} attaining a speed of 450 km s^{-1} at 16 R$_\odot$. However, in the extended *STA* FOV up to 38 R$_\odot$, the CME decelerates at 0.82 ms^{-2}. Since the driving force during the flare impulsive phase is weak, the CME decelerates during the propagation phase. The PE launched type III bursts delayed by 14 min with respect to the flare peak time (04:58 UT). Our analysis reveals that the type III bursts originated due to post-flare reconnection but not during the flare impulsive phase. Depending on the strength of the flare, the electrons are very likely to emerge out as type III during the flare impulsive period.

This study of PE indicates that the magnetic reconnection plays prime role on the CME speed, which then launch type II, III burst with the onset of the eruption in the source regions. It also constrains
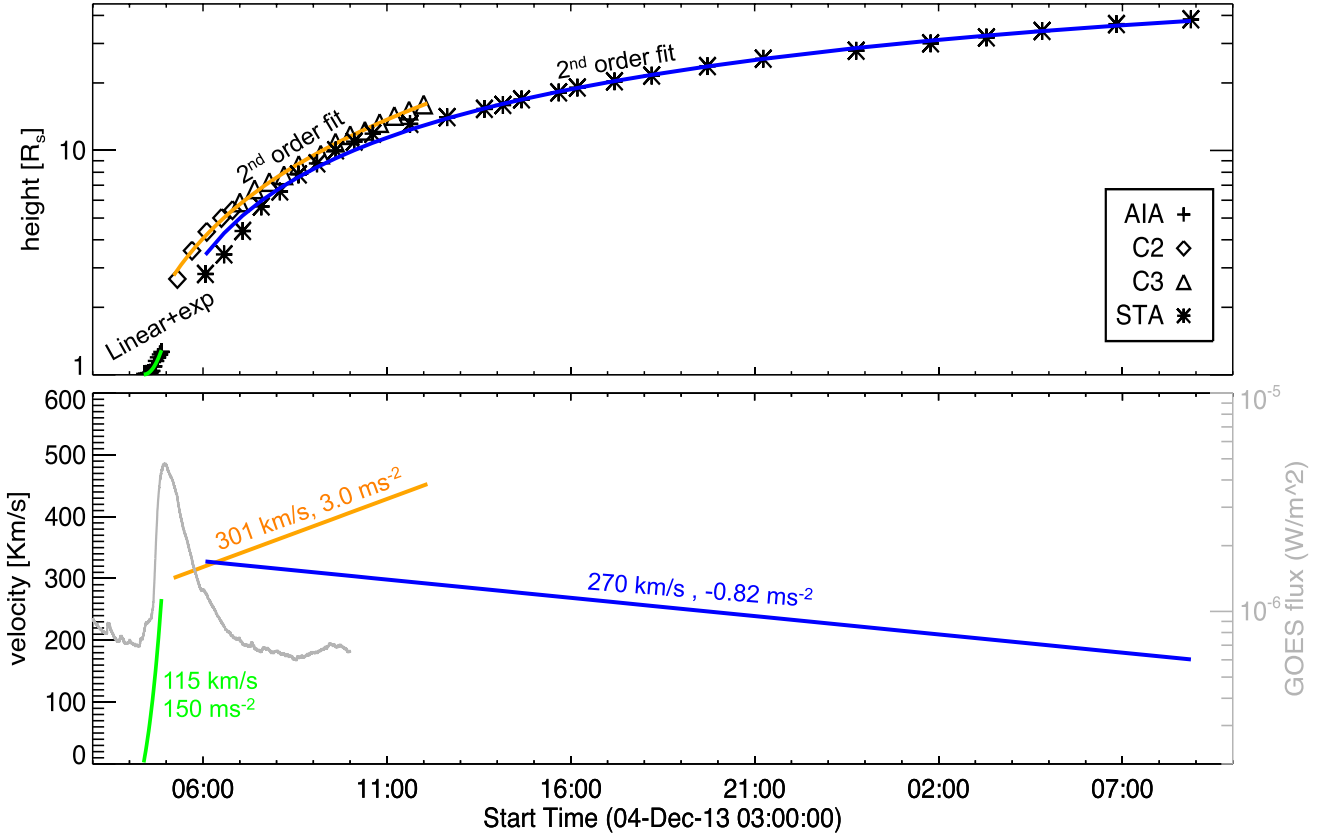
Figure 9. The kinematics of prominence and its CME. *Top panel*: height–time plot of the erupting prominence in the AIA FOV (indicated with ' + ' symbol), the CME LE in the LASCO FOV (diamond and triangle symbols) and the leading edge in *STA* FOV ('∗' symbol). The heights are obtained in the plane of sky. The green curve is the model fit including linear and exponential terms. Orange and blue curves are the model fits to the height–time data of LASCO and *STA* with a second-order polynomial function. *Bottom panel*: the derived velocities from the model fits to the height–time data. GOES X-ray flux is also shown with y-axis scale on right. Average velocity and acceleration are shown with each fitting. In AIA FOV, the prominence rises with rapid acceleration which is also in sync with rise of the GOES flux. In LASCO, the CME velocity increases from 300 to 453 km s^{-1} at 3 ms^{-2}, whereas *STA* measurements delineate that the CME decelerates at 0.82 ms^{-2}.

the CME propagation distance farther away from the Sun. More such detailed studies are helpful to shed light on the effect of source region characteristics on the CME propagation.

DATA AVAILABILITY

The data used in this manuscript are obtained from NASA's *SDO* mission and is publicly available from Joint Science Op-

erations Center (http://jsoc.stanford.edu/). GONG Hα is accessed from (https://gong2.nso.edu/archive/patch.pl?menutype = hAlpha). *STEREO/SECCHI* data are obtained from Stereo Science Center (http://https://stereo-ssc.nascom.nasa.gov/data/ins_data/secchi/L 0/a/img/). *SOHO* LASCO data and related information for the event of interest in this study are accessed from (https://cdaw.gsfc.nasa.g ov/CME_list/UNIVERSAL_ver1/2013_12/univ2013_12.html.)

REFERENCES

Alexander D., Liu R., Gilbert H. R., 2006, ApJ, 653, 719
Amari T., Luciani J. F., Aly J. J., et al, 2003, ApJ, 585, 1073
Antiochos S. K., DeVore C. R., Klimchuk J. A., 1999, ApJ, 510, 485
Bougeret J. L. et al., 1995, Space Sci. Rev., 71, 231
Brueckner G. E. et al., 1995, Sol. Phys., 162, 357
Cane H. V., Sheeley N. R. J., Howard R. A., 1987, J. Geophys. Res., 92, 9869
Canfield R. C., Hudson H. S., McKenzie D. E., 1999, Geophys. Res. Lett., 26, 627
Chen P. F., 2011, Liv. Rev. Sol. Phys., 8, 1
Cheng X., Zhang J., Ding M. D., Olmedo O., Sun X. D., Guo Y., Liu Y., 2013, ApJ, 769, L25
Davies J. A. et al., 2009, Geophys. Res. Lett., 36, L02102
Filippov B., 2013, ApJ, 773, 10
Filippov B. P., Den O. G., 2001, J. Geophys. Res., 106, 25177
Forbes T. G., Isenberg P. A., 1991, ApJ, 373, 294

Gibson S. E., 2018, Liv. Rev. Sol. Phys., 15, 7

Gilbert H. R., Alexander D., Liu R., 2007, Sol. Phys., 245, 287

Gopalswamy N., Shimojo M., Lu W., Yashiro S., Shibasaki K., Howard R. A., 2003, ApJ, 586, 562

Gopalswamy N., Mäkelä P., Yashiro S., 2019, Sun and Geosphere, 14, 111

Green L. M., Kliem B., Török T., van Driel-Gesztelyi L., Attrill G. D. R., 2007, Sol. Phys., 246, 365

Howard R. A., Moses J. D., Vourlidas A., Newmark J. S., et al, 2008, Space Sci. Rev., 136, 67

Illing R. M. E., Hundhausen A. J., 1985, J. Geophys. Res., 90, 275

Kaiser M. L., Kucera T. A., Davila J. M., St. Cyr O. C., Guhathakurta M., Christian E., 2008, Space Sci. Rev., 136, 5

Kishore P., Kathiravan C., Ramesh R., Rajalingam M., Barve I. V., 2014, Sol. Phys., 289, 3995

Kliem B., Török T., 2006, Phys. Rev. Lett., 96, 255002

Kliem B., Titov V. S., Török T., 2004, A&A, 413, L23

Lemen J. R. et al., 2012, Sol. Phys., 275, 17

Lin J., Soon W., Baliunas S. L., 2003, New A Rev., 47, 53

Mackay D. H., Karpen J. T., Ballester J. L., Schmieder B., Aulanier G., 2010, Space Sci. Rev., 151, 333

Mahender A., Sasikumar Raja K., Ramesh R., Panditi V., Monstein C., Ganji Y., 2020, Sol. Phys., 295, 153

Martin S. F., 1998, in Webb D. F., Schmieder B., Rust D. M., eds, ASP Conf. Ser. Vol. 150, IAU Colloq. 167: New Perspectives on Solar Prominences. p. 419, available at: https://ui.adsabs.harvard.edu/abs/1998ASPC..150.419M/exportcitation

Melrose D. B., 1980, Space Sci. Rev., 26, 3

Moore R. L., Sterling A. C., Hudson H. S., Lemen J. R., 2001a, ApJ, 552, 833

Moore R. L., Sterling A. C., Hudson H. S., Lemen J. R., 2001b, ApJ, 552, 833

Priest E. R., Forbes T. G., 2002, A&A Rev., 10, 313

Rust D. M., Kumar A., 1994, Sol. Phys., 155, 69

Rust D. M., Kumar A., 1996, ApJ, 464, L199

Shanmugaraju A., Moon Y. J., Dryer M., Umapathy S., 2003, Sol. Phys., 215, 185

Sheeley N. R., Walters J. H., Wang Y. M., Howard R. A., 1999, J. Geophys. Res., 104, 24739

Song H. Q., Chen Y., Zhang J., Cheng X., Fu H. LI G., 2015, ApJ, 804, L38

Song H. Q., Y. Chen, J. Zhang, Cheng X., Wang B., HU Q., LI G., Wang Y. M., 2015, ApJ, 808, L15

Song H. Q., Chen Y., Qiu J., Chen C. X., Zhang J., Cheng X., Shen Y. D., Zheng R. S., 2018, ApJ, 857, L21

Török T., Kliem B., Titov V. S., 2004, A&A, 413, L27

van Ballegooijen A. A., Martens P. C. H., 1989, ApJ, 343, 971

Vasanth V., Chen Y., Feng S., et al, 2016, ApJ, 830, L2

Vasantharaju N., Vemareddy P., Ravindra B., Doddamani V. H., 2018, ApJ, 860, 58

Vasantharaju N., Vemareddy P., Ravindra B., Doddamani V. H., 2019a, ApJ, 874, 182

Vasantharaju N., Vemareddy P., Ravindra B., Doddamani V. H., 2019b, ApJ, 885, 89

Vemareddy P., Zhang J., 2014, ApJ, 797, 80

Vemareddy P., Maurya R. A., Ambastha A., 2012, Sol. Phys., 277, 337

Vemareddy P., Gopalswamy N., Ravindra B., 2017, ApJ, 850, 38

Vemareddy P., Démoulin P., Sasikumar Raja K., Zhang J., Gopalswamy N., Vasantharaju N., 2022, ApJ, 927, 108

Vršnak B., 2016, Astronomische Nachrichten, 337, 1002

Vršnak B., Ruždjak D., Sudar D., Gopalswamy N., 2004, A&A, 423, 717

Webb D. F., Howard T. A., 2012, Liv. Rev. Sol. Phys., 9, 3

Webb D. F., Hundhausen A. J., 1987, Sol. Phys., 108, 383

Zhang J., Dere K. P., Howard R. A., Kundu M. R., White S. M., 2001, ApJ, 559, 452

Zhang J., Cheng X., Ding M.-D., 2012, Nat. Commun., 3 , 747

Zhang J. et al, 2021, Prog. Earth Planet Sci., 8, 56

This paper has been typeset from a TEX/LATEX file prepared by the author.